

# Edge states in all-dielectric square-lattice arrays of bianisotropic microwave resonators

Alina D. Rozenblit,<sup>1,\*</sup> Georgiy D. Kurganov,<sup>1</sup> and Nikita A. Olekhno<sup>1</sup>

<sup>1</sup>*School of Physics and Engineering, ITMO University,  
49 Kronverksky pr., bldg. A, 197101 Saint Petersburg, Russia*

(Dated: June 24, 2024)

We demonstrate that a bianisotropic response associated with a broken mirror symmetry of a dielectric resonator allows opening the bandgap in simple square lattice arrays of such resonators. Realizing the proposed system as an array of high-index ceramic resonators working at GHz frequencies, we numerically and experimentally demonstrate the presence of edge states at the interface between two domains with opposite orientations of the bianisotropic resonators as well as at the boundary between a single domain and free space. For both cases, we characterize the dispersion of edge states, examine their propagation along sharp bends, their resilience towards various types of geometrical defects, and a spin-momentum locked unidirectional propagation in the case of circularly polarized excitation. The considered design opens novel possibilities in constructing optical and microwave structures simultaneously featuring edge states at the interfaces between distinct resonator domains or a resonator domain and free space.

## I. INTRODUCTION

Edge and surface states propagating along the interfaces of media with distinct topological properties [1, 2] demonstrate a set of fascinating physical phenomena related to their topological protection, including bulk-boundary correspondence [3], resilience towards geometrical imperfections in the structure [4], and the absence of backscattering at sharp bends [5–8].

Such states have been demonstrated experimentally with a plethora of platforms including acoustic [9] and microwave systems [10], electrical circuits with either passive [11] or active components [12], and mechanical systems [13], including those with actively moving particles [14] or robots [15]. Among the recent trends are reconfigurable platforms both in acoustics [16] and infrared optics [17]. Moreover, photonic topological edge states have promising practical applications at frequencies from microwave to optical. In particular, such excitations may help to eliminate the necessity of impedance matching between the feed lines and antenna arrays [18] due to the absence of back-reflection, as well as allow realizing a miniature on-chip phase shifters [19] and enhance the radiation efficiency of a waveguide to free space in THz domain [20].

Recently, setups based on coupled all-dielectric resonators became widespread both in microwave [21–23] and optical [4] experiments owing to their low loss levels, with high-index ceramic cylinders being a prominent example in microwaves. One of the approaches to implement topological phenomena in arrays of such resonators utilizes their individual bianisotropy, which can be introduced by breaking the inversion symmetry of the resonator's shape [24, 25]. The emerging hybridization of the electric and magnetic modes represents the analog of spin-orbit interaction in quantum systems, and leads to

the bandgap opening [6, 21, 26].

While two-dimensional [7] (2D) and three-dimensional [27] (3D) hexagonal lattices of dielectric bianisotropic particles featuring Dirac dispersion are well studied, the systems with such particles arranged in a square lattice remain unexplored experimentally, with only lossy metallic counterparts at hand [6, 28]. Besides, edge and corner-localized topological states have been demonstrated in square lattices with unconventionally selected unit cell [29], including the case when the lattice is formed by magneto-optic rods [30]. Moreover, square-lattice systems implementing different topological models are extensively realized as electrical circuits [31–33] and photonic setups [34–38].

In this article, we study experimentally and describe theoretically a 2D array of ceramic bianisotropic resonators placed at the sites of a simple square lattice which supports edge-localized states, Fig. 1. The introduced

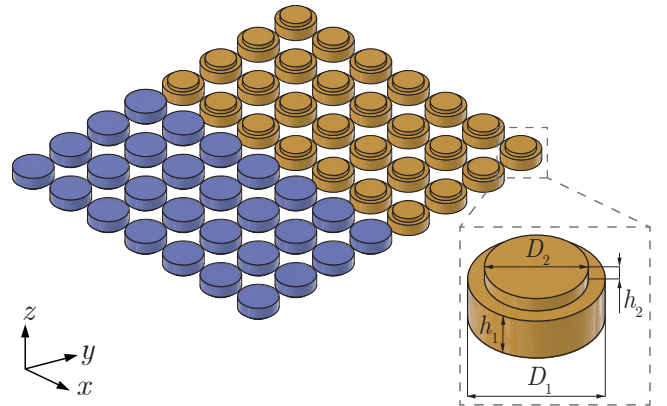


Figure 1. The schematics of the proposed photonic topological insulator including an interface between two arrays of oppositely oriented bianisotropic resonators forming a square lattice. The color of the bianisotropic resonators highlights their orientation. The inset shows an individual resonator with characteristic dimensions specified.

\* [alina.rozenblit@metalab.ifmo.ru](mailto:alina.rozenblit@metalab.ifmo.ru)

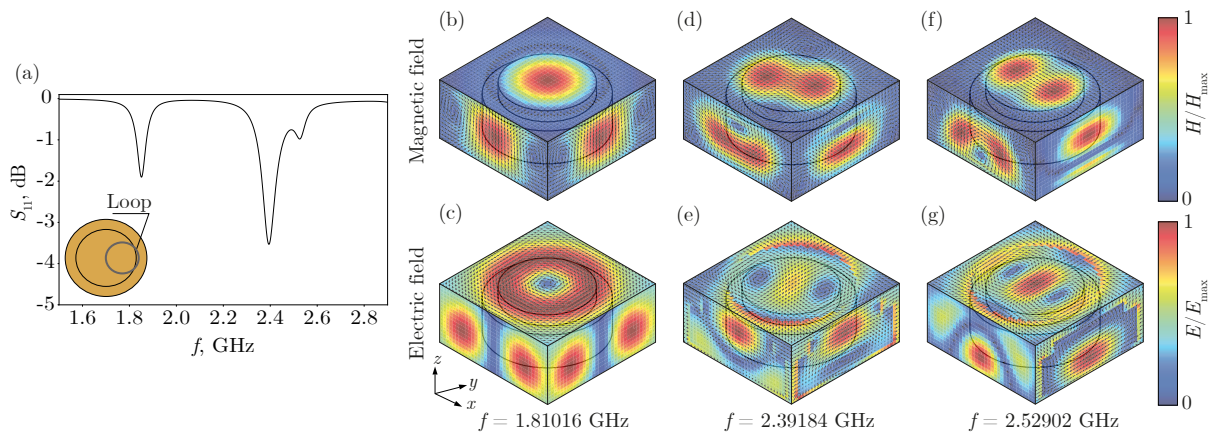


Figure 2. (a) Numerically calculated  $S_{11}$ -parameter for an individual bianisotropic resonator. The inset shows the position of the loop antenna in the numerical model. (b-g) Magnetic and electric field distributions at the three orthogonal central cross-sections of the bianisotropic resonator at the frequencies of (b,c)  $f = 1.81016$  GHz, (d,e)  $f = 2.39184$  GHz, and (f,g)  $f = 2.52902$  GHz, respectively. For visual clarity, the cross-sections are translated to the facets of a box enclosing the resonator. The color shows the normalized absolute value of the magnetic or electric fields, while the black arrows visualize the tangential components of the magnetic or electric fields in the respective planes.

system is essentially a single layer of the model theoretically considered in Ref. [39]. We demonstrate the presence of edge states at the interface between two lattice domains with oppositely orientated resonators, as well as at the interface between a single lattice domain and free space. Moreover, we study spin-momentum locking of such states in the case of circularly polarized excitation, and show that they propagate robustly along the sharp bends.

The paper is organized as follows. In Section II, we study numerically an individual bianisotropic resonator and discuss numerical simulations for an infinite square lattice of resonators. Then, in Section III, we present experimental results for edge states at the interface between two bianisotropic domains as well as at the free space – single domain interface, considering their dispersion, spin-momentum locking, and propagation along sharp bends. Effective Hamiltonian and topological properties of the considered model are analysed in Section IV. Section V contains a discussion of the results and an outlook.

## II. THE STRUCTURE AND PROPERTIES OF BIANISOTROPIC PLANAR ARRAY

We start with studying the properties of a single bianisotropic resonator with CST Microwave Studio 2022 software package. The resonator is implemented as two concentrically attached cylinders with the diameters  $D_1 = 29.1$  mm and  $D_2 = 22$  mm and the heights  $h_1 = 9$  mm and  $h_2 = 3$  mm, respectively, Fig. 1. The symmetry axes of the cylinders are aligned with the  $z$ -axis of the coordinate system. The permittivity of the resonator's material is set to  $\epsilon = 39$ , while the loss angle is  $\delta = 0.0001$  at the frequency  $f = 2.43$  GHz. The resonator is located in vacuum with  $\epsilon = 1$ .

To characterize numerically the resonant spectrum of the bianisotropic resonator, we introduce a loop antenna with the diameter 12 mm implemented as a torus made of a 0.4 mm thick perfect electric conductor wire and placed atop the resonator at the height of 1 mm, as shown in the inset of Fig. 2(a). Then, we evaluate the frequency dependence of  $S_{11}$ -parameter using Frequency Domain Solver. As seen from the obtained spectrum in Fig. 2(a), the resonator features resonances at the frequencies close to  $f = 1.85$  GHz,  $f = 2.39$  GHz, and  $f = 2.53$  GHz. The same procedure is implemented experimentally for several resonators having the same dimensions and material properties to characterize their spectra, as discussed in Supplemental Material [40].

Next, with the help of Eigenvalue Solver, we visualize the spatial distributions of the magnetic and electric field amplitudes in three orthogonal planes passing through the center of the resonator for each of the discussed resonances, Fig. 2(b-g). For visual clarity, the corresponding maps are shifted to the facets of the box incorporating the resonator. Each of the field profiles is normalized to the maximum value of its amplitude. The directions and in-plane amplitudes of tangential parts of the magnetic and electric fields in the corresponding planes are shown with black arrows, while the color denotes the total magnitude of the respective field.

The eigenstate at the frequency  $f = 1.81016$  GHz clearly represents a magnetic dipole, i.e., a current loop in the  $(xy)$ -plane, Fig. 2(b,c). In particular, it is seen that the  $z$ -component of magnetic field is maximal and nearly uniform at the symmetry axis of the resonator, while the  $z$ -component of electric field vanishes. In turn, the in-plane  $(xy)$ -component of the electric field is directed tangentially to the cylinder surface, characteristic of a current loop in the  $(xy)$ -plane. At higher frequencies  $f = 2.39184$  GHz and  $f = 2.52902$  GHz, the eigenstates

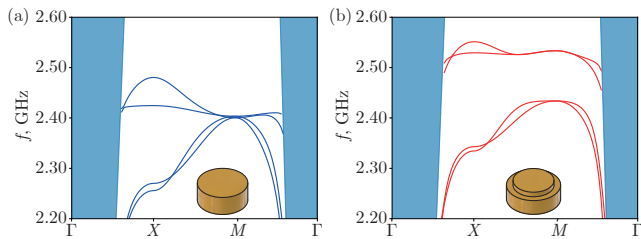


Figure 3. (a) Dispersion diagram for the infinite 2D square lattice consisting of dielectric cylinders. The shaded area shows the light cone, and the inset demonstrates the geometry of a single cylinder. (b) The same as panel (a), but for the infinite array of bianisotropic resonators.

shown in Fig. 2(d,e) and Fig. 2(f,g) render as combinations of electric and magnetic dipolar modes.

Next, we apply Floquet boundary conditions to the model of a cylindrical resonator composed of ceramics with the permittivity  $\epsilon = 39$  and having the diameter  $D = D_1 = 29.1$  mm and the height  $h = h_1 + h_2 = 12$  mm to simulate an infinite 2D square lattice with the period  $a = 37.1$  mm, which corresponds to the 8 mm distance between the resonators' edges. The obtained dispersion diagram shown in Fig. 3(a) demonstrates the absence of a bandgap in such a lattice. However, for the same lattice of considered bianisotropic resonators a bandgap ranging from nearly 2.43 GHz to 2.53 GHz at the  $M$ -point is observed, see Fig. 3(b). This highlights the crucial role of the bianisotropy in the emergence of topological edge states.

### III. EXPERIMENTAL RESULTS

#### A. Two-domain configurations

In the experiments, we consider resonators composed of MgO-CaO-TiO<sub>2</sub> ceramics with the same dimensions and permittivity as in the numerical simulations, and arrange them in a square lattice of either  $13 \times 14$  or  $14 \times 14$  resonators in the horizontal plane with the period  $a = 37.1$  mm in an extruded polystyrene foam (XPS) substrate, Fig. 4(a). In the following, we start with a finite structure composed of two oppositely-oriented square-lattice arrays of bianisotropic resonators, Fig. 1.

First, we characterize the transmission between two subwavelength dipole antennas, the transmitting and the receiving ones, by measuring the  $S_{21}$ -parameter with PLANAR C4490 vector network analyzer (VNA) and Agilent 83020A microwave amplifier attached to the transmitting antenna. In the first case, the transmitter and the receiver are placed in the bulk of the lattice, red line in Fig. 4(b), and a considerable decrease in the transmission is observed at the frequencies between 2.42 GHz and 2.51 GHz, facilitating the presence of a bandgap. In the second scenario, we place the antennas at the interface

between two lattices with opposite orientations of the resonators, blue line in Fig. 4(b). It is seen that no damping is observed in the bandgap region, which highlights the possible excitation of the interface-localized states.

In further experiments, we characterize a near-field distribution of the vertical component of magnetic field with the XF-R 3-1 H-field probe (the subwavelength loop antenna) while exciting the structure with the subwavelength dipole antenna. Both antennas are attached to Rohde & Schwarz ZVB-20 VNA, and the measurements are conducted with the automatic Trim TMC 3113 scanner. The scanner step is set to  $\Delta = 2.5$  mm for both directions in the horizontal plane.

To experimentally characterize the dispersion of interface states, we evaluate the dynamic structure parameter (DSF) applying discrete Fourier transform to the  $S_{21}$  parameters extracted along the domain wall, while the source antenna is put at the edge of interface, see Supplementary Materials for details [40]. The obtained normalized DSF in Fig. 4(c) demonstrates the emergence of the interface-localized excitation in the bandgap. The comparison of the extracted dispersion with the light cone  $f = ck/2\pi a$ , where  $c$  is the speed of light, shows that a considerable part of the edge state dispersion curve lies below the light cone. Thus, such edge states should not effectively radiate to free space.

Next, we perform a near-field scanning of the whole structure with the size  $14 \times 13$  cylinders and a linear interface Fig. 4(d). The obtained magnetic field profile for the linear source polarization at the frequency  $f = 2.47$  GHz shown in Fig. 4(e) demonstrates a strong confinement of magnetic fields to the interface localized in both directions from the transmitting antenna, in agreement with the results in Fig. 4(b,c).

Next, we test the spin-momentum locking of the observed edge states under a circularly-polarized excitation. In such a case, either destructive or constructive interference of the fields allows achieving a unidirectional wave propagation [41]. To emulate a circularly polarized excitation, we repeat the measurements twice for orthogonal dipole antenna positions and subsequently add or subtract the field profiles with a  $\pi/2$  phase shift. It is seen that the considered system supports unidirectional wave propagation upon the excitation by a left-handed [Fig.4(f)] and right-handed [Fig.4(g)] circularly polarized sources at frequency  $f = 2.47$  GHz, which can be treated as spin-up and spin-down modes. Such ability to guide the wave unidirectionally as well as switch the direction of its propagation renders useful from the practical point of view.

To study the robustness of the edge states to the sharp bends in the interface geometry, we consider an array of  $14 \times 14$  resonators with a double-bend (zigzag) interface, Fig. 4(h). In analogy to the case with a linear domain wall, we perform scanning with linear and circular source polarizations. The obtained distributions at the frequency  $f = 2.47$  GHz closely resemble those measured for the linear interface configuration, Fig. 4(i-k). In par-

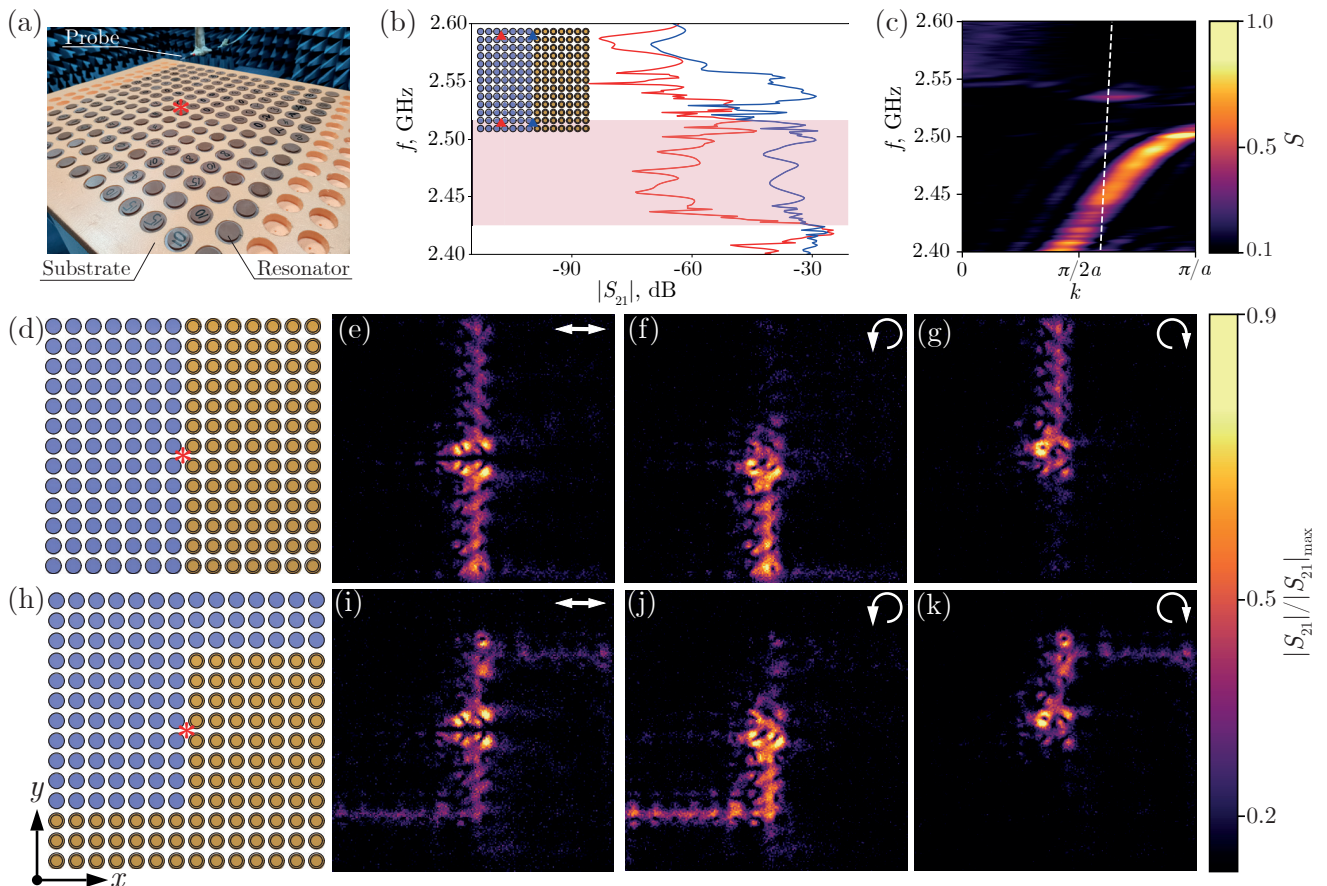


Figure 4. (a) Photo of the considered system implemented as an array of ceramic resonators placed in an extruded polystyrene foam substrate. (b) Transmission between two dipole antennas in the the bulk (red solid line) and at the interface (blue solid line). (c) Experimentally obtained dispersion (dynamic structure factor) for the interface state. The white dashed line shows the light cone. (d) Schematics of the configuration with a linear domain wall. (e-g) Experimentally measured magnetic fields at  $f = 2.47$  GHz for the structure with a linear domain wall in the cases of (e) linear, (f) left-handed circular, and (g) right-handed circular polarization of the excitation. (h-k) The same as (d-g), but for a double-bend domain wall. The red asterisk in panels (a,d,h) indicates the position of the dipole subwavelength source antenna.

ticular, a pronounced localization at the interface is observed for a linearly-polarized excitation [Fig. 4(i)], while circularly-polarized excitation results in a unidirectional propagation along the interface bend [Fig. 4(j,k)].

## B. Single-domain configurations

As we demonstrate further, an interesting property of the considered structure is that it supports edge states at the interface between the resonator array and free space as well. Analogous states have been previously predicted for the photonic gyrotropic square-lattice topological insulators [42] and studied in valley photonic topological insulators systems to realize frequency multiplexing in waveguides [43]. To demonstrate such states, we consider a single domain consisting of  $12 \times 7$  resonators, Fig. 5(a). In a full analogy to the previously studies interface between domains with opposite orientations of

the resonators, we evaluate DSF [Fig. 5(b)] and characterize magnetic field distributions in the case of a linearly polarized source [Fig. 5(c)] and left- or right-handed circular polarizations [Fig. 5(d,e)], respectively. While the localization of the edge state and spin-momentum locking closely resemble those for the interface between two domains, Fig. 4(e-g), the edge state dispersion in Fig. 5(b) is more concentrated above the light cone, facilitating more radiative nature of such states, and demonstrates nearly flat shape below the light cone, characteristic of lower group velocity compared to the nearly linear behavior of DSF in Fig. 4(c).

Next, we implement a double-band single-domain configuration, Fig. 5(f), and characterize its magnetic field response. When the system is excited by a subwavelength dipole antenna the magnetic field concentrating at the cylinders nearest to the free space region is able to envelope the angle with vertex  $B$ , which is not observed for the angle with vertex  $C$ . Moreover, the field

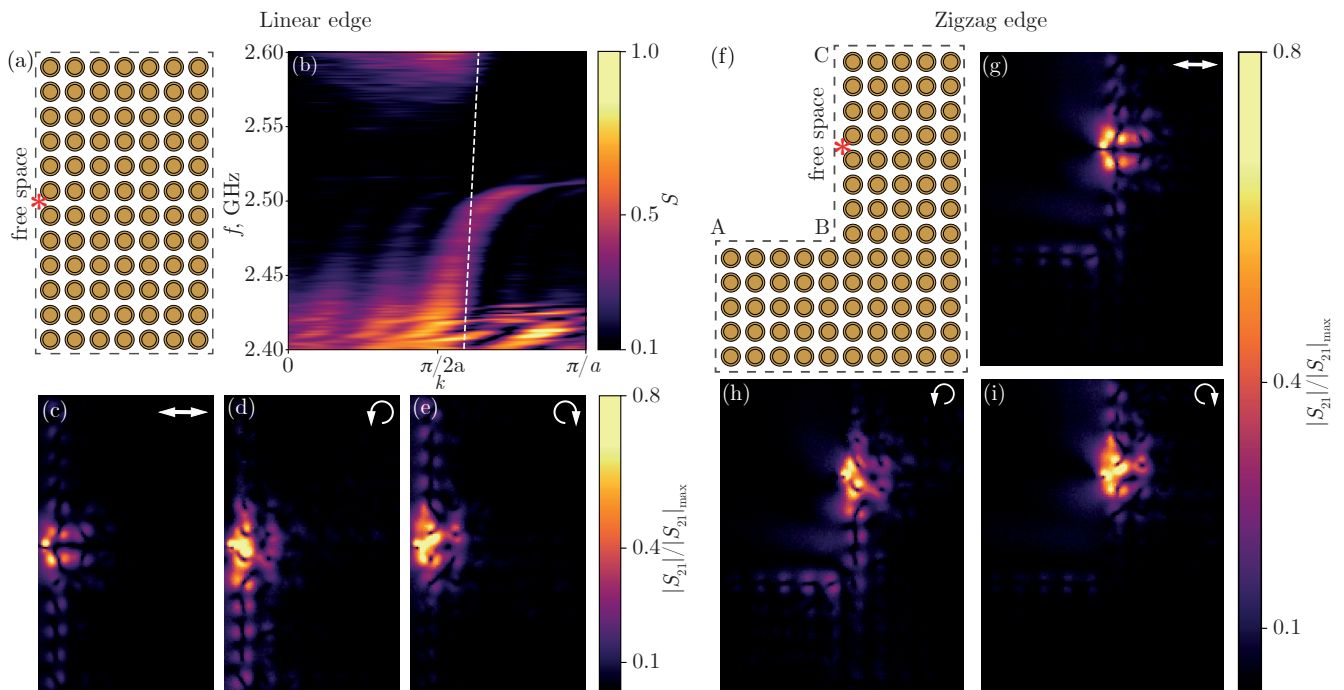


Figure 5. (a) Schematics of the single-domain configuration with a linear boundary. The red asterisk marks the position of the source antenna and the grey dashed line denotes the boundary between the domain with bianisotropic resonators and free space. (b) Experimentally obtained dispersion diagram for the states at the boundary between the domain and free space. The white dashed line shows the light cone. (c)-(e) Magnetic field profiles extracted at the frequency  $f = 2.455$  GHz in the case of the sources with (c) linear, (d) left-handed circular, and (e) right-handed circular polarizations. (f) Schematics of the single-domain configuration with a double-bend (zigzag) boundary. The red asterisk marks the position of the source antenna and the grey dashed line corresponds to the boundary between the domain and free space. (g)-(i) Magnetic field profiles extracted at the frequency  $f = 2.455$  GHz for sources with (g) linear, (h) left-handed circular, and (i) right-handed circular polarizations.

drastically fades before reaching the vertex  $A$ , Fig. 5(g). The same effect is observed for the system excited by left- and right-handed circularly polarized sources, while a single way propagation it still observed, Fig. 5(h,i). In Supplementary Materials [40] we also provide experimental results for disordered geometries with extracted resonators at the interface, which highlight that edge states lack robustness towards such point defects.

Finally, it is worth noting that a considerable portion of edge state dispersion both for the two-domain configuration Fig. 4(c) and especially for a single-domain configuration Fig. 5(b) is above the light cone. Indeed, it is seen that the experimentally obtained magnetic field profiles at the frequency  $f = 2.455$  GHz possess energy radiation in free space [Fig. 6(a)], while the fields at the frequency  $f = 2.480$  GHz localize inside the structure and demonstrate more pronounced coupling with bulk excitations, as the frequency of such a state is close to the bulk spectrum [Fig. 6(b)].

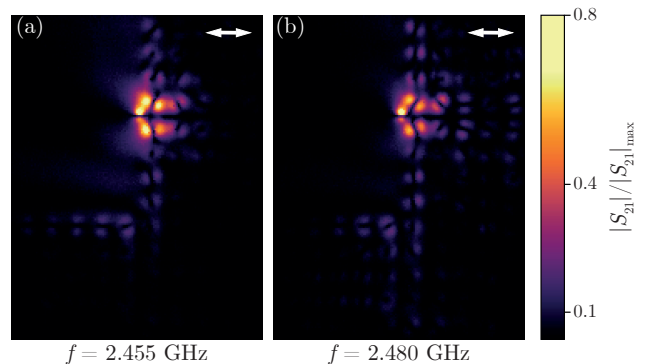


Figure 6. Experimentally obtained magnetic field profiles for the single-domain configuration with the zigzag edge excited by a linearly polarized source at the frequency (a)  $f = 2.455$  GHz and (b)  $f = 2.480$  GHz.

#### IV. HAMILTONIAN AND BAND TOPOLOGY

According to the electric and magnetic field distributions of a single bianisotropic resonator [Fig. 2], in the frequency range from 2.39 GHz to 2.53 GHz the system can be considered as an array of coupled electric and

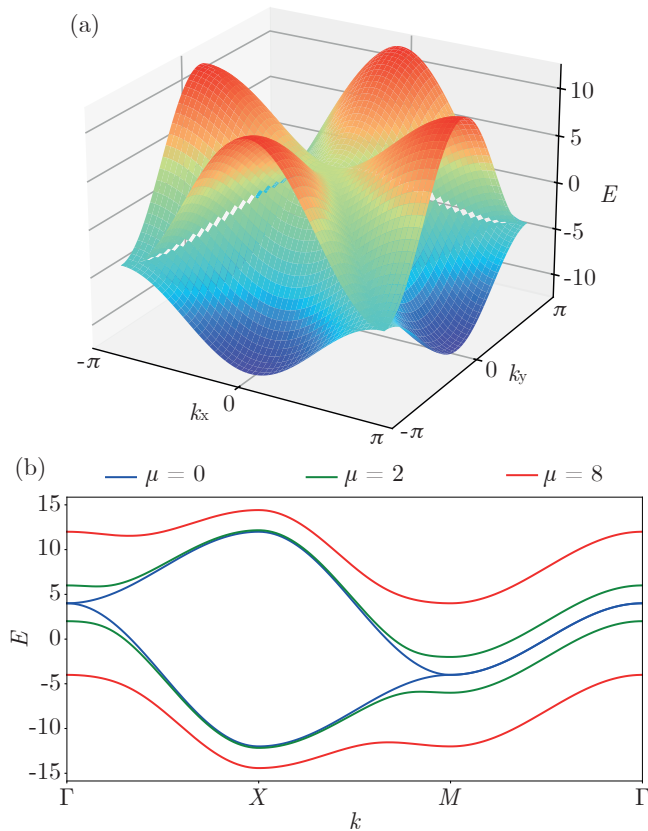


Figure 7. (a) Eigenenergy bands (Eq. 2) in the case of absent bianisotropy  $\mu = 0$ . Color shows the value of  $E(k)$ . (b) The dispersion diagrams for the eigenvalues  $E(k)$  of the derived Hamiltonian Eq. (2) for the wavenumber  $k = (k_x, k_y)$  varied along the  $\Gamma - X - M - \Gamma$  trajectory in the reciprocal space for different values of the bianisotropy  $\mu = 0$  (blue solid line),  $\mu = 2$  (green solid line), and  $\mu = 8$  (red solid line), respectively.

magnetic point dipoles located in the  $(xy)$ -plane. To devise the theoretical model, we rely on the dyadic Green's function approach outlined for a one-dimensional chain of bianisotropic resonators in Ref. [21]. Besides, we apply the tight-binding approximation considering only the interactions between the nearest resonators.

Within such an approach, each resonator is characterized by a four-component vector of its in-plane electric  $p_{x,y}$  and magnetic  $m_{x,y}$  moments, correspondingly, which naturally group into spin-like basis:  $|\psi\rangle = (p_x + im_y, p_x - im_y, p_y - im_x, p_y + im_x)^T$ . Within such a basis, the effective Bloch Hamiltonian  $\hat{H}(k_x, k_y)$  for an infinite 2D square lattice array of resonators takes the following form:

$$\hat{H}(k_x, k_y) = 2(\cos k_x + \cos k_y)\hat{I} \otimes \hat{I} - 2\mu\hat{I} \otimes \hat{\sigma}_z + 6(\cos k_x - \cos k_y)\hat{\sigma}_z \otimes \hat{\sigma}_x = \begin{pmatrix} \hat{H}^{(+)} & 0 \\ 0 & \hat{H}^{(-)} \end{pmatrix}, \quad (1)$$

where  $\hat{I}$  is the  $[2 \times 2]$  unity matrix,  $\hat{\sigma}_x = (0, 1; 1, 0)$  and  $\hat{\sigma}_z = (1, 0; 0, -1)$  are Pauli matrices, the parameter  $\mu$

characterizes the strength of the bianisotropic coupling of electric and magnetic moments, and  $k_{x,y}$  are the in-plane components of the wavenumber. Diagonal  $[2 \times 2]$  blocks  $\hat{H}^{(+)}$  and  $\hat{H}^{(-)}$  describe two Kramers degenerate partners analogous to spin-up and spin-down states in the selected basis and share the same set of eigenvalues. The Bloch Hamiltonian derivation is detailed in Supplemental Material [40]. Such a Hamiltonian thus features two doubly degenerate bands of eigenenergies  $\hat{H}(k_x, k_y)|\psi\rangle = E(k_x, k_y)|\psi\rangle$ :

$$E^{(\pm)}(k_x, k_y) = 2(\cos k_x + \cos k_y) \pm \sqrt{36(\cos k_x - \cos k_y)^2 + \mu^2}, \quad (2)$$

which are visualized for arrays without bianisotropy ( $\mu = 0$ ) in Fig. 7(a). Also, it is seen from Eq. (2) that for  $k_x = \pm k_y$  all bands become fourfold degenerate, and the bandgap quadratically closes along the  $\Gamma - M$  line, with  $\Gamma = (0, 0)$ ,  $X = (\pi, 0)$ , and  $M = (\pi, \pi)$  being high-symmetry points of the Brillouin zone, see Fig. 7(b). However, adding a bianisotropy  $\mu > 0$  eliminates such a degeneracy, resulting in a bandgap opening for every  $k$ , see the example for  $\mu = 2$  in Fig. 7(b). Finally, for sufficiently large  $\mu$ , a complete bandgap is observed, shown in Fig. 7(b) for  $\mu = 8$ . Eigenfunctions of the Hamiltonian Eq. (1) have the following form:

$$\begin{aligned} |\psi\rangle_1^- &= \left( \frac{\mu - \sqrt{9A^2(k_x, k_y) + \mu^2}}{3A(k_x, k_y)}, 1, 0, 0 \right)^T, \\ |\psi\rangle_2^- &= \left( 0, 0, \frac{-\mu + \sqrt{9A^2(k_x, k_y) + \mu^2}}{3A(k_x, k_y)}, 1 \right)^T, \\ |\psi\rangle_1^+ &= \left( \frac{\mu + \sqrt{9A^2(k_x, k_y) + \mu^2}}{3A(k_x, k_y)}, 1, 0, 0 \right)^T, \\ |\psi\rangle_2^+ &= \left( 0, 0, \frac{-\mu - \sqrt{9A^2(k_x, k_y) + \mu^2}}{3A(k_x, k_y)}, 1 \right)^T, \end{aligned} \quad (3)$$

where  $A(k_x, k_y) = \cos k_x - \cos k_y$  is the antisymmetric combination of cosine functions, upper indices ( $\pm$ ) denote the corresponding energy branch from Eq. (2), and lower indices correspond to two degenerate eigenvalues.

Considering previously demonstrated spin-locking and robust propagation of the in-gap edge states in experiments, as well as the form of Bloch Hamiltonian Eq. (1), the question naturally arises if the emerging bandgap is topological, and the considered system supports photonic quantum spin-Hall phase similar to the ones reported in Refs. [7, 27, 44]. Since the considered system possesses time-reversal symmetry, Chern numbers of upper and lower bands vanish, and the relevant invariants are either spin Chern numbers  $C_\uparrow$  and  $C_\downarrow$  calculated separately for spin-up and spin-down states in the respective band or  $Z_2$  invariant [45]. However, a direct evaluation of Berry curvature for eigenfunctions Eq. (3) shows that it zeroes out, in consistency with the evaluation of  $Z_2$  invariant for the Hamiltonian Eq. (1) with the help of

Z2PACK [46] which yields  $Z_2 = 0$ . Thus, the considered Hamiltonian is topologically trivial. The observed edge states then might represent 1D photonic analogs of Jackiw-Rebbi edge states [21, 27], as the Hamiltonian Eq. (1) naturally generalizes the model of Ref. [21] from 1D linear arrays to 2D square lattices.

## V. DISCUSSION

To conclude, we have numerically and experimentally demonstrated the emergence of edge states at microwave frequencies supported by a simple square lattice of resonators and governed by their individual bianisotropy. The demonstrated phenomena include spin-momentum locking of such states at the interface between two distinct domains and their resilience towards geometrical imperfections. All of the reported effects are also observed at the boundary between a single domain and free space, up to a slight modification of the edge state dispersion. The considered system has zero  $Z_2$  invariant, and thus rather hosts photonic analogs of Jackiw-Rebbi

interface states [21, 27].

As directions for further development, thermal [23] or mechanical [47] reconfigurability may be introduced to the considered structures to engineer such edge states. The other prospective avenue is to consider three-phase arrays composed of resonator domains with different signs of bianisotropy as well as free space or domains consisting of resonators without a pronounced bianisotropy. Such systems have been considered in Ref. [48] for realizing on-chip THz waveguides. It also appears intriguing to address nonlinear effects [4, 49–51] and to quantify the effects of long-range interactions [22, 52] in the considered model. Finally, the observed phenomena can be realized in optical domain by miniaturizing the resonators [53].

## ACKNOWLEDGMENTS

We acknowledge fruitful discussions with Maxim Gorlach. The work was financially supported by the Russian Science Foundation (project 21-79-10209).

- 
- [1] L. Lu, J. D. Joannopoulos, and M. Soljačić, Topological photonics, *Nature photonics* **8**, 821 (2014).
  - [2] T. Ozawa, H. M. Price, A. Amo, N. Goldman, M. Hafezi, L. Lu, M. C. Rechtsman, D. Schuster, J. Simon, O. Zeitlinger, and I. Carusotto, Topological photonics, *Reviews of Modern Physics* **91**, 015006 (2019).
  - [3] M. G. Silveirinha, Bulk-edge correspondence for topological photonic continua, *Physical Review B* **94**, 205105 (2016).
  - [4] S. Kruk, A. Poddubny, D. Smirnova, L. Wang, A. Slobozhanyuk, A. Shorokhov, I. Kravchenko, B. Luther-Davies, and Y. Kivshar, Nonlinear light generation in topological nanostructures, *Nature nanotechnology* **14**, 126 (2019).
  - [5] Z. Wang, Y. Chong, J. D. Joannopoulos, and M. Soljačić, Observation of unidirectional backscattering-immune topological electromagnetic states, *Nature* **461**, 772 (2009).
  - [6] A. P. Slobozhanyuk, A. B. Khanikaev, D. S. Filonov, D. A. Smirnova, A. E. Miroschnichenko, and Y. S. Kivshar, Experimental demonstration of topological effects in bianisotropic metamaterials, *Scientific reports* **6**, 22270 (2016).
  - [7] A. Slobozhanyuk, A. V. Shchelokova, X. Ni, S. Hossain Mousavi, D. A. Smirnova, P. A. Belov, A. Alù, Y. S. Kivshar, and A. B. Khanikaev, Near-field imaging of spin-locked edge states in all-dielectric topological metasurfaces, *Applied Physics Letters* **114**, 031103 (2019).
  - [8] Y. Wang, H.-X. Wang, L. Liang, W. Zhu, L. Fan, Z.-K. Lin, F. Li, X. Zhang, P.-G. Luan, Y. Poo, *et al.*, Hybrid topological photonic crystals, *Nature Communications* **14**, 4457 (2023).
  - [9] X. Ni, M. A. Gorlach, A. Alu, and A. B. Khanikaev, Topological edge states in acoustic kagome lattices, *New Journal of Physics* **19**, 055002 (2017).
  - [10] Y. Li, Y. Sun, W. Zhu, Z. Guo, J. Jiang, T. Kariyado, H. Chen, and X. Hu, Topological LC-circuits based on microstrips and observation of electromagnetic modes with orbital angular momentum, *Nature Communications* **9**, 4598 (2018).
  - [11] M. Serra-Garcia, R. Süssstrunk, and S. D. Huber, Observation of quadrupole transitions and edge mode topology in an LC circuit network, *Physical Review B* **99**, 020304 (2019).
  - [12] T. Kotwal, F. Moseley, A. Stegmaier, S. Imhof, H. Brand, T. Kießling, R. Thomale, H. Ronellenfitsch, and J. Dunkel, Active topoelectrical circuits, *Proceedings of the National Academy of Sciences* **118**, e2106411118 (2021).
  - [13] R. Süssstrunk and S. D. Huber, Observation of phononic helical edge states in a mechanical topological insulator, *Science* **349**, 47 (2015).
  - [14] S. Shankar, A. Souslov, M. J. Bowick, M. C. Marchetti, and V. Vitelli, Topological active matter, *Nature Reviews Physics* **4**, 380 (2022).
  - [15] X. Yang, C. Ren, K. Cheng, and H. Zhang, Robust boundary flow in chiral active fluid, *Physical Review E* **101**, 022603 (2020).
  - [16] A. Darabi, M. Collet, and M. J. Leamy, Experimental realization of a reconfigurable electroacoustic topological insulator, *Proceedings of the National Academy of Sciences* **117**, 16138 (2020).
  - [17] M. B. On, F. Ashtiani, D. Sanchez-Jacome, D. Perez-Lopez, S. B. Yoo, and A. Blanco-Redondo, Programmable integrated photonics for topological Hamiltonians, *Nature Communications* **15**, 629 (2024).
  - [18] Y. Lumer and N. Engheta, Topological insulator antenna arrays, *ACS Photonics* **7**, 2244 (2020).

- [19] H. Wang, G. Tang, Y. He, Z. Wang, X. Li, L. Sun, Y. Zhang, L. Yuan, J. Dong, and Y. Su, Ultracompact topological photonic switch based on valley-vortex-enhanced high-efficiency phase shift, *Light: Science & Applications* **11**, 292 (2022).
- [20] R. Jia, S. Kumar, T. C. Tan, A. Kumar, Y. J. Tan, M. Gupta, P. Szriftgiser, A. Alphones, G. Ducournau, and R. Singh, Valley-conserved topological integrated antenna for 100-Gbps THz 6G wireless, *Science Advances* **9**, eadi8500 (2023).
- [21] A. A. Gorlach, D. V. Zhirihin, A. P. Slobozhanyuk, A. B. Khanikaev, and M. A. Gorlach, Photonic Jackiw-Rebbi states in all-dielectric structures controlled by bianisotropy, *Physical Review B* **99**, 205122 (2019).
- [22] M. Li, D. Zhirihin, M. Gorlach, X. Ni, D. Filonov, A. Slobozhanyuk, A. Alù, and A. B. Khanikaev, Higher-order topological states in photonic kagome crystals with long-range interactions, *Nature Photonics* **14**, 89 (2020).
- [23] G. Kurganov, D. Dobrykh, E. Puhtina, I. Yusupov, A. Slobozhanyuk, Y. S. Kivshar, and D. Zhirihin, Temperature control of electromagnetic topological edge states, *Applied Physics Letters* **120** (2022).
- [24] R. Alaee, M. Albooyeh, A. Rahimzadegan, M. S. Mirmoosa, Y. S. Kivshar, and C. Rockstuhl, All-dielectric reciprocal bianisotropic nanoparticles, *Physical Review B* **92**, 245130 (2015).
- [25] S. H. Mousavi, A. B. Khanikaev, and Z. Wang, Topologically protected elastic waves in phononic metamaterials, *Nature communications* **6**, 8682 (2015).
- [26] D. A. Bobylev, D. A. Smirnova, and M. A. Gorlach, Photonic topological states mediated by staggered bianisotropy, *Laser & Photonics Reviews* **15**, 1900392 (2021).
- [27] A. Slobozhanyuk, S. H. Mousavi, X. Ni, D. Smirnova, Y. S. Kivshar, and A. B. Khanikaev, Three-dimensional all-dielectric photonic topological insulator, *Nature Photonics* **11**, 130 (2017).
- [28] D. A. Bobylev, D. I. Tikhonenko, A. B. Khanikaev, M. A. Gorlach, and D. V. Zhirihin, Observation of topological corner states in a D4-symmetric square lattice of splitting resonators, *Applied Physics Letters* **122** (2023).
- [29] Y. Chen, Z. Lan, and J. Zhu, Second-order topological phases in C4v-symmetric photonic crystals beyond the two-dimensional Su-Schrieffer-Heeger model, *Nanophotonics* **11**, 1345 (2022).
- [30] Z. Lan, Y. Chen, L. An, and Z. Su, Chern, dipole, and quadrupole topological phases of a simple magneto-optical photonic crystal with a square lattice and an unconventional unit cell, *Physical Review B* **109**, 045402 (2024).
- [31] N. A. Olekhno, E. I. Kretov, A. A. Stepanenko, P. A. Ivanova, V. V. Yaroshenko, E. M. Puhtina, D. S. Filonov, B. Cappello, L. Matekovits, and M. A. Gorlach, Topological edge states of interacting photon pairs emulated in a topoelectrical circuit, *Nature communications* **11**, 1436 (2020).
- [32] N. A. Olekhno, A. D. Rozenblit, V. I. Kachin, A. A. Dmitriev, O. I. Burmistrov, P. S. Seregin, D. V. Zhirihin, and M. A. Gorlach, Experimental realization of topological corner states in long-range-coupled electrical circuits, *Physical Review B* **105**, L081107 (2022).
- [33] S. Liu, W. Gao, Q. Zhang, S. Ma, L. Zhang, C. Liu, Y. J. Xiang, T. J. Cui, and S. Zhang, Topologically protected edge state in two-dimensional Su-Schrieffer-Heeger circuit, *Research* (2019).
- [34] X.-D. Chen, D. Zhao, X.-S. Zhu, F.-L. Shi, H. Liu, J.-C. Lu, M. Chen, and J.-W. Dong, Edge states in self-complementary checkerboard photonic crystals: Zak phase, surface impedance, and experimental verification, *Physical Review A* **97**, 013831 (2018).
- [35] Y. Ota, F. Liu, R. Katsumi, K. Watanabe, K. Wakabayashi, Y. Arakawa, and S. Iwamoto, Photonic crystal nanocavity based on a topological corner state, *Optica* **6**, 786 (2019).
- [36] B.-Y. Xie, G.-X. Su, H.-F. Wang, H. Su, X.-P. Shen, P. Zhan, M.-H. Lu, Z.-L. Wang, and Y.-F. Chen, Visualization of higher-order topological insulating phases in two-dimensional dielectric photonic crystals, *Physical Review Letters* **122**, 233903 (2019).
- [37] X.-D. Chen, W.-M. Deng, F.-L. Shi, F.-L. Zhao, M. Chen, and J.-W. Dong, Direct observation of corner states in second-order topological photonic crystal slabs, *Physical Review Letters* **122**, 233902 (2019).
- [38] C. Han, M. Kang, and H. Jeon, Lasing at multidimensional topological states in a two-dimensional photonic crystal structure, *ACS Photonics* **7**, 2027 (2020).
- [39] T. Ochiai, Gapless surface states originating from accidentally degenerate quadratic band touching in a three-dimensional tetragonal photonic crystal, *Physical Review A* **96**, 043842 (2017).
- [40] See Supplemental Material at [URL] for (i) the details of numerical simulations for unit cell and supercell models; (ii) experimental studies of disorder in the properties of individual resonators and the edge states propagation with point-like defects; (iii) derivation of the Bloch Hamiltonian; (iv) details of the dispersion evaluation from experimental measurements.
- [41] F. J. Rodríguez-Fortuño, G. Marino, P. Ginzburg, D. O'Connor, A. Martínez, G. A. Wurtz, and A. V. Zayats, Near-field interference for the unidirectional excitation of electromagnetic guided modes, *Science* **340**, 328 (2013).
- [42] A. C. Tasolamprou, M. Kafesaki, C. M. Soukoulis, E. N. Economou, and T. Koschny, Chiral topological surface states on a finite square photonic crystal bounded by air, *Physical Review Applied* **16**, 044011 (2021).
- [43] G. Wei, Z. Liu, H. Wu, L. Wang, S. Wang, and J. Xiao, Boundary configured chiral edge states in valley topological photonic crystal, *Optics Letters* **47**, 3007 (2022).
- [44] A. B. Khanikaev, S. Hossein Mousavi, W.-K. Tse, M. Kargarian, A. H. MacDonald, and G. Shvets, Photonic topological insulators, *Nature materials* **12**, 233 (2013).
- [45] L. Fu and C. L. Kane, Topological insulators with inversion symmetry, *Physical Review B* **76**, 045302 (2007).
- [46] D. Gresch, G. Autes, O. V. Yazyev, M. Troyer, D. Vanderbilt, B. A. Bernevig, and A. A. Soluyanov, Z2Pack: Numerical implementation of hybrid wannier centers for identifying topological materials, *Physical Review B* **95**, 075146 (2017).
- [47] Q. Xu, X. Su, X. Zhang, L. Dong, L. Liu, Y. Shi, Q. Wang, M. Kang, A. Alù, S. Zhang, *et al.*, Mechanically reprogrammable Pancharatnam-Berry metasurface for microwaves, *Advanced Photonics* **4**, 016002 (2022).
- [48] W. Li, Q. Chen, Y. Sun, S. Han, X. Liu, Z. Mei, X. Xu, S. Fan, Z. Qian, H. Chen, *et al.*, Topologically enabled on-chip THz taper-free waveguides, *Advanced Optical Materials* **11**, 2300764 (2023).



- [49] S. Mittal, E. A. Goldschmidt, and M. Hafezi, A topological source of quantum light, *Nature* **561**, 502 (2018).
- [50] G. D'Aguanno, Y. Hadad, D. Smirnova, X. Ni, A. Khanikaev, and A. Alù, Nonlinear topological transitions over a metasurface, *Physical Review B* **100**, 214310 (2019).
- [51] D. Smirnova, D. Leykam, Y. Chong, and Y. Kivshar, Nonlinear topological photonics, *Applied Physics Reviews* **7** (2020).
- [52] A. Vakulenko, S. Kiriushechkina, M. Wang, M. Li, D. Zhirihin, X. Ni, S. Guddala, D. Korobkin, A. Alù, and A. B. Khanikaev, Near-field characterization of higher-order topological photonic states at optical frequencies, *Advanced Materials* , 2004376 (2021).
- [53] D. V. Zhirihin and Y. S. Kivshar, Topological photonics on a small scale, *Small Science* **1**, 2100065 (2021).

## Supplemental Material

### Edge states in all-dielectric square-lattice arrays of bianisotropic microwave resonators

Alina D. Rozenblit,<sup>1,\*</sup> Georgiy D. Kurganov,<sup>1</sup> and Nikita A. Olekhno<sup>1</sup>

<sup>1</sup>*School of Physics and Engineering, ITMO University,  
49 Kronverksky pr., bldg. A, 197101 Saint Petersburg, Russia*

(Dated: June 24, 2024)

#### CONTENTS

Supplementary Note 1. Numerical model and simulation results	1
Supplementary Note 2. Robustness to structural disorder	1
Supplementary Note 3. Bloch Hamiltonian derivation	4
Supplementary Note 4. Experimental evaluation of the dispersion diagram	7
References	7

#### SUPPLEMENTARY NOTE 1. NUMERICAL MODEL AND SIMULATION RESULTS

*Unit cell simulations.* For the simulations of the infinite array of bianisotropic resonators, we use Eigenvalue solver applied to the unit cell under Floquet boundary conditions along the  $x$ - and  $y$ -axes, while both  $k_x$  and  $k_y$  wavevectors change along  $\Gamma - X - M - \Gamma$  trajectory in the reciprocal space between the high-symmetry points of the Brillouin zone. The dispersion diagrams obtained for the infinite array of bianisotropic and cylindrical resonators with period  $a = 37.1$  mm are shown in Fig. 1(a,b) in the main text.

*Supercell simulations.* The supercell numerical model includes two 1D domains with opposite orientations of resonators placed along the  $x$ -axis and separated by a spacing  $d$  between the domains. Each domain includes seven resonators. In this case, Floquet boundary conditions are also set in both  $x$ - and  $y$ -directions. However, the wavenumber along the  $x$ -axis of the supercell is set to  $k_x = 0$  corresponding to periodic boundary conditions, while the wavenumber  $k_y$  is varied from 0 to  $\pi$ . Note, that such an approach leads to the emergence of an additional boundary interface associated with periodic boundary conditions. In the following, we select only the modes corresponding to the central interface, increase the distance between the domains, and finally replace one of them with a vacuum media. The latter model allows us to search for the modes featuring energy localization along the interface between the topological insulator and free space.

The obtained dispersion diagram for  $d = a$  shown in Fig. S1(a) demonstrates the existence of three isolated curves corresponding to the in-gap edge states, with two of them (the black and red curves) being close to the bulk bands. When the distance between the domains increases to  $d = 1.5a$ , just two types of states are observed, as one of the initial states merges into the upper bulk band, Fig. S1(b). For  $d = 2a$ , only a single type of edge states exists, as the red branch merges to the lower bulk continuum, Fig. S1(c). At the same time, the states at the green branch corresponding to the experimentally observed states [Fig. 4(c) in the main text] shift upwards upon the increase of spacing between the domains, and, finally, in the supercell with a single domain just a slight tail of these modes remains below the light cone, Fig. S1(d). In experiments, we do not observe the states corresponding to the black and red branches due to their hybridization with the bulk modes.

#### SUPPLEMENTARY NOTE 2. ROBUSTNESS TO STRUCTURAL DISORDER

*The resonant frequency.* According to the numerical results, the considered dielectric bianisotropic resonators possess two resonant peaks at frequencies  $f = 2.39$  GHz and  $f = 2.53$  GHz corresponding to the coupled electric

---

\* [alina.rozenblit@metalab.ifmo.ru](mailto:alina.rozenblit@metalab.ifmo.ru)

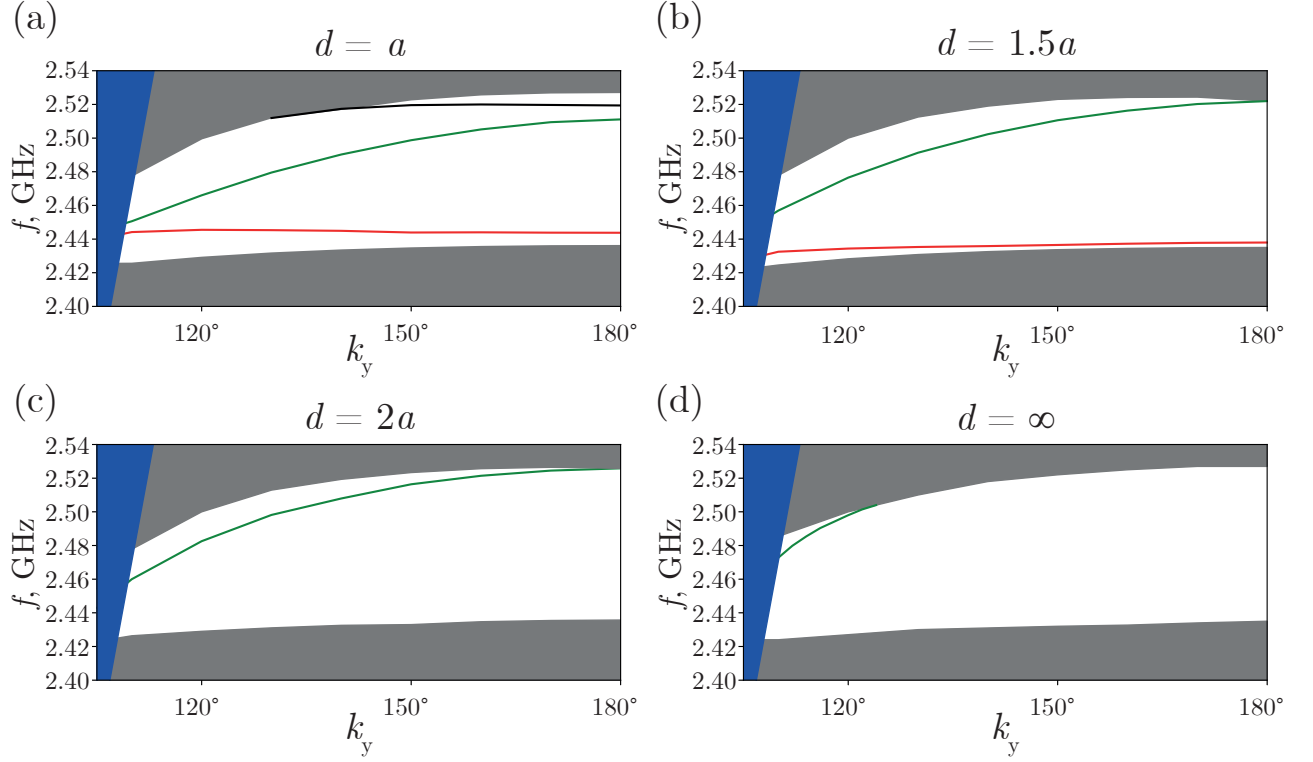


Figure S1. Dispersion diagrams for supercells with different distances  $d$  between the domains with opposite signs of bianisotropy for (a)  $d = a$ , (b)  $d = 1.5a$ , and (c)  $d = 2a$ , where  $a$  is the in-domain lattice constant. (d) Dispersion diagram for the supercell consisting of a single domain and vacuum media replacing the domain with opposite orientation of resonators, equivalent to the infinite separation between the domains  $d = \infty$ . The grey and blue shaded areas correspond to the bulk bands and radiation continuum above the light cone, respectively. The black, grey, and red curves indicate the modes with electromagnetic fields localized at the interfaces between two domains or between the domain and vacuum media.

and magnetic dipole moments. However, actual resonant frequencies of the resonators in the experimental setup deviate from the idealized values due to manufacturing imperfections. Thus, we measure  $S_{11}$ -parameters with the help of the loop antenna having the diameter 12 mm for the 50 randomly chosen resonators. The position of the loop antenna is the same as in the numerical simulations (inset in Fig. 2(a) in the main text). These measurements are carried out using PLANAR C4490 vector network analyzer. The obtained  $S_{11}$  spectra are shown in Fig. S2. To evaluate the resonances distribution, we focus at the second resonant peak considering the range from 2.475 GHz to 2.600 GHz. The average frequency of the resonant peak in the mentioned frequency range is 2.501 GHz, and the frequency deviation for different resonators ranges from 2.493 to 2.520 GHz. Within the experiments, we arrange the resonators in the following way: the greater the distance from a considered resonator and the interface for two-domain configurations or the studied boundary in the single-domain cases, the larger is frequency detuning of the resonator.

*Interface between two domains.* To introduce the imperfections in the two-domain system with a linear interface, we consider the structure of  $14 \times 13$  resonators and remove a pair of resonators, one at each side of the interface, Fig. S3(a). The measurement results for linearly and circularly polarized sources are shown in Fig. S3(b-c). In experiments, we measure near fields only in the area of interest to optimize the scanning time. Experimental results demonstrate that the edge state continues to localize at the interface. However, the magnetic field amplitude drastically decreases after the imperfection, facilitating the strong character of such a defect.

*Interface between the domain and free space.* Similarly to the interface configuration with disorder discussed before, we remove one resonator at the edge of the single-domain configuration, Fig. S3(d). The the magnetic field profiles at the frequencies of the edge states  $f = 2.455$  [Fig. S3(e,g)] and upper bulk region  $f = 2.505$  [Fig. S3(f,h)] facilitate that edge state cannot propagate through such a defect, in contrast to bulk modes.

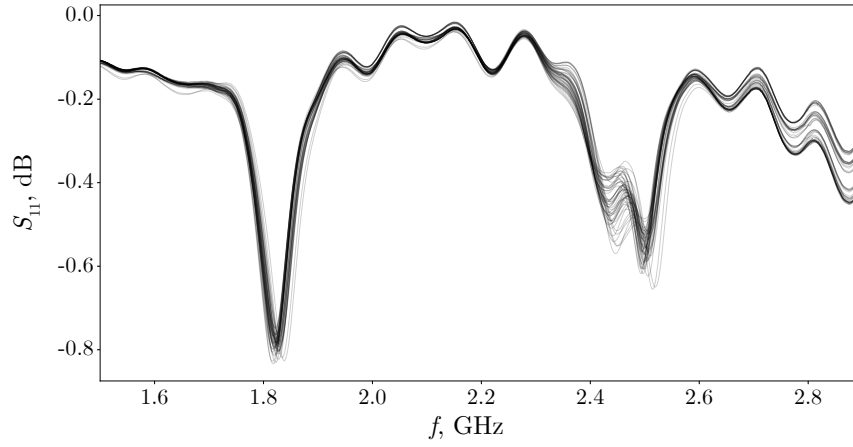


Figure S2. Experimentally measured  $S_{11}$ -parameters spectra for 50 bianisotropic resonators.

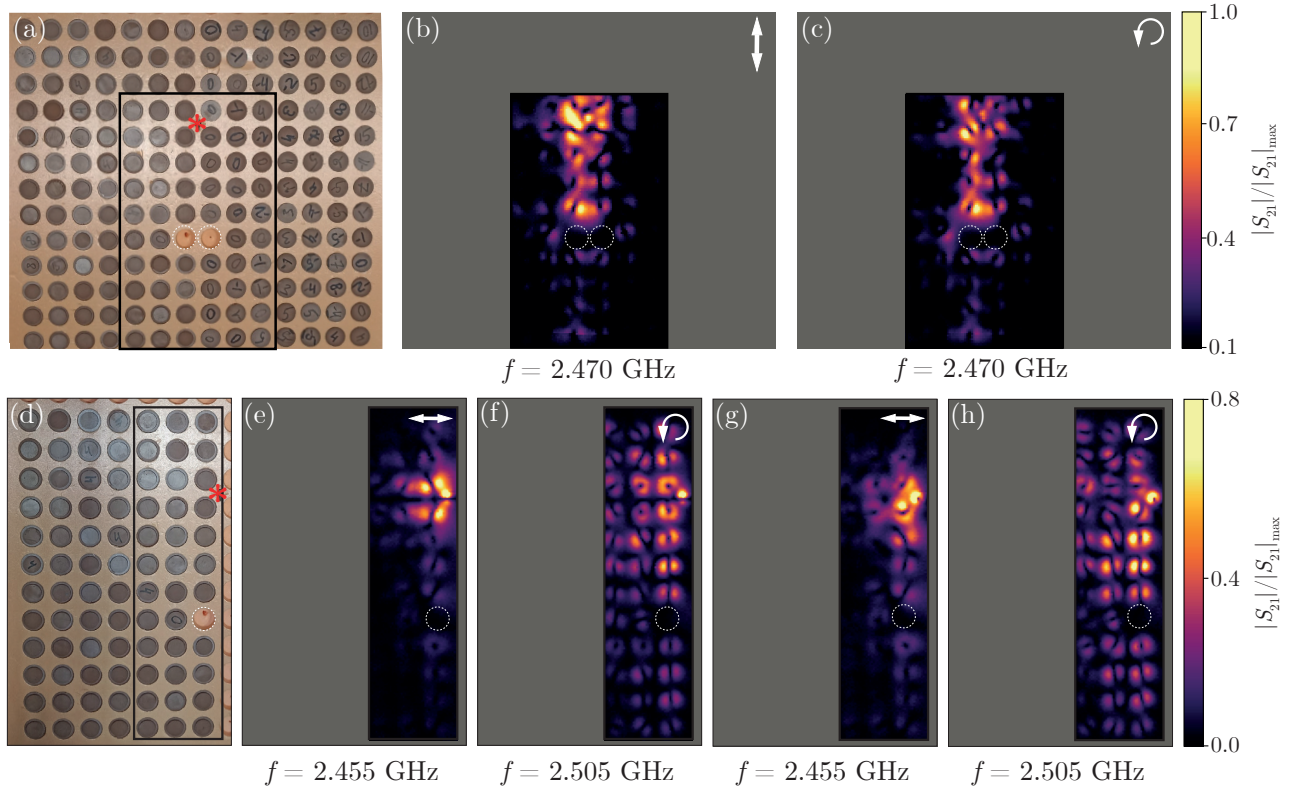


Figure S3. (a) Photo of the experimental setup featuring a linear domain wall with an extracted pair of resonators at the interface. The black frame shows the scanning area and the red asterisk denotes the position of a subwavelength source dipole antenna. (b,c) The measured transmission coefficient profiles at the frequency  $f = 2.470$  GHz for linear and circular source polarizations, respectively. (d) Photo of the one-domain configuration without a resonator at the boundary. The black frame corresponds to the scanning area and the red asterisk denotes the position of a source dipole subwavelength antenna. (e,f) Experimentally measured magnetic field profiles in case of linear polarization excitation at the frequency of the edge state  $f = 2.455$  GHz and scattering in the bulk  $f = 2.505$  GHz, respectively. (g,h) The same as panels (e,f), but for the left-handed polarization excitation. The white dashed circles shows the position of the removed resonator.

**SUPPLEMENTARY NOTE 3. BLOCH HAMILTONIAN DERIVATION**

To derive the Bloch Hamiltonian describing a square lattice of bianisotropic resonators, we apply the approach from Ref. [1]. First, we establish the following assumptions concerning the frequencies of the electromagnetic hybridization (2.39 - 2.53 GHz) obtained from numerical simulations (Fig. 1 in the main text):

1. The considered system may be represented as a two-dimensional array of point magnetic and electric dipoles. For simplicity, we assume the resulting electric and magnetic field amplitudes in the resonators to be equal.
2. In the frequency range of the bianisotropic modes, the resonators possess electric and magnetic dipoles in the  $xy$ -plane, as the height of resonators is considerably smaller than their diameter, which results in larger frequencies of dipolar modes along the  $z$ -axis.
3. Each resonator interacts only with its nearest neighbors.

The components of the electric ( $p$ ) and magnetic ( $m$ ) dipole moments are related with components of the electric and magnetic fields of the resonator at the lattice site ( $n, l$ ) via the polarizability tensor  $\hat{\alpha}$ :

$$\begin{pmatrix} p_x^{nl} \\ p_y^{nl} \\ m_x^{nl} \\ m_y^{nl} \end{pmatrix} = \hat{\alpha} \begin{pmatrix} E_x^{nl} \\ E_y^{nl} \\ H_x^{nl} \\ H_y^{nl} \end{pmatrix}. \quad (1)$$

The polarizability tensor can be decomposed into electric  $\hat{\alpha}^{ee}$ , magnetic  $\hat{\alpha}^{mm}$ , electro-magnetic  $\hat{\alpha}^{em}$ , and magneto-electric  $\hat{\alpha}^{me}$  parts, each being a  $[2 \times 2]$  matrix:

$$\hat{\alpha} = \begin{pmatrix} \hat{\alpha}^{ee} & \hat{\alpha}^{em} \\ \hat{\alpha}^{me} & \hat{\alpha}^{mm} \end{pmatrix}. \quad (2)$$

We assume that the polarizabilities of the magnetic and electric dipoles are equal, while the polarizability along  $z$ -axis is neglected:

$$\hat{\alpha}^{ee} = \hat{\alpha}^{mm} = \begin{pmatrix} \beta & 0 \\ 0 & \beta \end{pmatrix}. \quad (3)$$

The bianisotropic parts of the polarizability tensor are defined as

$$\hat{\alpha}^{em} = \hat{\alpha}^{me} = \begin{pmatrix} 0 & i\chi \\ -i\chi & 0 \end{pmatrix}, \quad (4)$$

where  $\chi$  is the coupling of the electric and magnetic dipoles. Thus, the polarizability tensor has the following form:

$$\hat{\alpha} = \begin{pmatrix} \beta & 0 & 0 & i\chi \\ 0 & \beta & -i\chi & 0 \\ 0 & i\chi & \beta & 0 \\ -i\chi & 0 & 0 & \beta \end{pmatrix}. \quad (5)$$

Now, the electric and magnetic field from Eq. (1) can be derived with the help of inverse polarizability tensor:

$$\hat{\alpha}^{-1} \begin{pmatrix} p_x^{nl} \\ p_y^{nl} \\ m_x^{nl} \\ m_y^{nl} \end{pmatrix} = \begin{pmatrix} u & 0 & 0 & -iv \\ 0 & u & iv & 0 \\ 0 & -iv & u & 0 \\ iv & 0 & 0 & u \end{pmatrix} \begin{pmatrix} p_x^{nl} \\ p_y^{nl} \\ m_x^{nl} \\ m_y^{nl} \end{pmatrix} = \begin{pmatrix} E_x^{nl} \\ E_y^{nl} \\ H_x^{nl} \\ H_y^{nl} \end{pmatrix}, \quad (6)$$

where  $u = \frac{\beta}{\beta^2 - \chi^2}$ , and  $v = \frac{\chi}{\beta^2 - \chi^2}$ .

On the other hand, the electromagnetic fields can be evaluated via the Green's functions for point dipoles:

$$\mathbf{E}^{nl} = \hat{G}^{ee}(r_{ij}, k_0) \mathbf{p}^{ij} + \hat{G}^{em}(r_{ij}, k_0) \mathbf{m}^{ij} \quad (7)$$

$$\mathbf{H}^{nl} = \hat{G}^{me}(r_{ij}, k_0) \mathbf{p}^{ij} + \hat{G}^{mm}(r_{ij}, k_0) \mathbf{m}^{ij} \quad (8)$$

where  $r_{ij}$  is the distance between the resonators with coordinates  $(n, l)$  and  $(i, j)$ ,  $k_0$  is the wavenumber, and the contribution of the electric dipole in the electric field is the same as the contribution of the magnetic dipole in the magnetic field  $\widehat{G}^{mm}(r_{ij}, k_0) = \widehat{G}^{ee}(r_{ij}, k_0)$ , while Green's functions for the bianisotropic parts are related as  $\widehat{G}^{em}(r_{ij}, k_0) = -\widehat{G}^{me}(r_{ij}, k_0)$ . Dyadic Green's function components can be expressed in the following manner:

$$\widehat{G}_{\zeta, \eta}^{ee} = (\partial_\zeta \partial_\eta + k_0^2 \delta_{\zeta, \eta}) \frac{e^{ik_0 r_{ij}}}{r_{ij}} \quad (9)$$

$$\widehat{G}_{\zeta, \eta}^{em} = ik_0 \varepsilon_{\zeta, \eta, \kappa} \partial_\kappa \frac{e^{ik_0 r_{ij}}}{r_{ij}} \quad (10)$$

where  $\delta_{\zeta, \eta}$  is the Kronecker delta,  $\varepsilon_{\zeta, \eta, \kappa}$  is Levi-Civita symbol, and  $\partial_\zeta = \frac{\partial}{\partial \zeta}$ . Parameters  $\zeta, \eta, \kappa$  take values  $\{x, y, z\}$

If the distance between the resonators  $r_{ij} = r = \sqrt{x^2 + y^2}$ , then, according to Eq. (9) and Eq. (10), the components of the dyadic Green's functions are

$$\widehat{G}_{xx}^{ee} = \frac{e^{ik_0 r}}{r^3} \left( \frac{x^2}{r^2} (3 - 3ik_0 r - k_0^2 r^2) + ik_0 r + k_0^2 r^2 - 1 \right), \quad (11)$$

$$\widehat{G}_{yy}^{ee} = \frac{e^{ik_0 r}}{r^3} \left( \frac{y^2}{r^2} (3 - 3ik_0 r - k_0^2 r^2) + ik_0 r + k_0^2 r^2 - 1 \right), \quad (12)$$

$$\widehat{G}_{xy}^{ee} = \widehat{G}_{yx}^{ee} = \frac{e^{ik_0 r}}{r^3} \left( \frac{xy}{r^2} (3 - 3ik_0 r - k_0^2 r^2) \right), \quad (13)$$

where  $x$  and  $y$  are the distances along the  $x$ - and  $y$ -axes, respectively. As the in-plane distance  $r$  is independent of the component  $\kappa = z$ , the function  $\widehat{G}_{\zeta, \eta}^{em} = 0$  for any combinations of  $\zeta$  and  $\eta$  for the considered system.

Next, we assume that the field of the particle with coordinates  $(n, l)$  is produced by the nearest resonators and introduce the summation over the rows and columns of the two-dimensional array of resonators:

$$\begin{aligned} \mathbf{E}^{nl} = & \sum_{i=n\pm 1, j=l} \widehat{G}^{ee}(r_{ij}, k_0) \mathbf{p}^{ij} + \sum_{i=n, j=m\pm 1} \widehat{G}^{ee}(r_{ij}, k_0) \mathbf{p}^{ij} \\ & + \sum_{i=n\pm 1, j=l} \widehat{G}^{em}(r_{ij}, k_0) \mathbf{m}^{ij} + \sum_{i=n, j=l\pm 1} \widehat{G}^{em}(r_{ij}, k_0) \mathbf{m}^{ij} \end{aligned} \quad (14)$$

$$\begin{aligned} \mathbf{H}^{nl} = & \sum_{i=n\pm 1, j=l} \widehat{G}^{ee}(r_{ij}, k_0) \mathbf{m}^{ij} + \sum_{i=n, j=l\pm 1} \widehat{G}^{ee}(r_{ij}, k_0) \mathbf{m}^{ij} \\ & - \sum_{i=n\pm 1, j=l} \widehat{G}^{em}(r_{ij}, k_0) \mathbf{p}^{ij} - \sum_{i=n, j=l\pm 1} \widehat{G}^{em}(r_{ij}, k_0) \mathbf{p}^{ij} \end{aligned} \quad (15)$$

Then, we rewrite Eqs. (11), (12), and (13) taking into account the lattice constant  $a$  ( $r = a$ ) and the coordinates  $i, j, n, l$ :

$$\widehat{G}_{xx}^{ee} = \frac{e^{ik_0 a}}{a^3} ((i-n)^2 (3 - 3ik_0 a - k_0^2 a^2) + ik_0 a + k_0^2 a^2 - 1) \quad (16)$$

$$\widehat{G}_{yy}^{ee} = \frac{e^{ik_0 a}}{a^3} ((j-l)^2 (3 - 3ik_0 a - k_0^2 a^2) + ik_0 a + k_0^2 a^2 - 1) \quad (17)$$

$$\widehat{G}_{xy}^{ee} = \widehat{G}_{yx}^{ee} = \frac{e^{ik_0 a}}{a^3} ((i-n)(j-l)(3 - 3ik_0 a - k_0^2 a^2)) \quad (18)$$

Now, these functions will be different for the sums along rows and columns in 2D array. If  $i = n \pm 1$  and  $j = l$ , then the dyadic Green's function are described in the following:

$$\begin{aligned} \widehat{G}_{xx}^{ee} &= A = 2 \frac{e^{ik_0 a}}{a^3} (1 - ik_0 a) \\ \widehat{G}_{yy}^{ee} &= B = \frac{e^{ik_0 a}}{a^3} (ik_0 a + k_0^2 a^2 - 1) \\ \widehat{G}_{xy}^{ee} &= \widehat{G}_{yx}^{ee} = 0 \end{aligned}$$

If  $i = n$  and  $j = l \pm 1$ :

$$\widehat{G}_{xx}^{ee} = B = \frac{e^{ik_0a}}{a^3} (ik_0a + k_0^2a^2 - 1) \quad (19)$$

$$\widehat{G}_{yy}^{ee} = A = 2 \frac{e^{ik_0a}}{a^3} (1 - ik_0a) \quad (20)$$

$$\widehat{G}_{xy}^{ee} = \widehat{G}_{yx}^{ee} = 0 \quad (21)$$

Finally, we can relate the electric and magnetic moments at the point with coordinates  $(n, l)$  Eq. (6), and  $(i, j)$  Eqs. (14), (15):

$$\begin{aligned} \widehat{\alpha}^{-1} \begin{pmatrix} p_x^{nl} \\ p_y^{nl} \\ m_x^{nl} \\ m_y^{nl} \end{pmatrix} &= \sum_{i=n\pm 1, j=l} \begin{pmatrix} G_{xx}^{ee} & G_{xy}^{ee} & G_{xx}^{em} & G_{xy}^{em} \\ G_{yx}^{ee} & G_{yy}^{ee} & G_{yx}^{em} & G_{yy}^{em} \\ -G_{xx}^{em} & -G_{xy}^{em} & G_{xx}^{ee} & G_{xy}^{ee} \\ -G_{yx}^{em} & -G_{yy}^{em} & G_{yx}^{ee} & G_{yy}^{ee} \end{pmatrix} \begin{pmatrix} p_x^{ij} \\ p_y^{ij} \\ m_x^{ij} \\ m_y^{ij} \end{pmatrix} \\ &+ \sum_{i=n, j=l\pm 1} \begin{pmatrix} G_{xx}^{ee} & G_{xy}^{ee} & G_{xx}^{em} & G_{xy}^{em} \\ G_{yx}^{ee} & G_{yy}^{ee} & G_{yx}^{em} & G_{yy}^{em} \\ -G_{xx}^{em} & -G_{xy}^{em} & G_{xx}^{ee} & G_{xy}^{ee} \\ -G_{yx}^{em} & -G_{yy}^{em} & G_{yx}^{ee} & G_{yy}^{ee} \end{pmatrix} \begin{pmatrix} p_x^{ij} \\ p_y^{ij} \\ m_x^{ij} \\ m_y^{ij} \end{pmatrix} \end{aligned} \quad (22)$$

Equation (22) can be rewritten as follows:

$$\widehat{\alpha}^{-1} \begin{pmatrix} p_x^{nl} \\ p_y^{nl} \\ m_x^{nl} \\ m_y^{nl} \end{pmatrix} = \sum_{i=n\pm 1, j=l} \begin{pmatrix} A & 0 & 0 & 0 \\ 0 & B & 0 & 0 \\ 0 & 0 & A & 0 \\ 0 & 0 & 0 & B \end{pmatrix} \begin{pmatrix} p_x^{ij} \\ p_y^{ij} \\ m_x^{ij} \\ m_y^{ij} \end{pmatrix} + \sum_{i=n, j=l\pm 1} \begin{pmatrix} B & 0 & 0 & 0 \\ 0 & A & 0 & 0 \\ 0 & 0 & B & 0 \\ 0 & 0 & 0 & A \end{pmatrix} \begin{pmatrix} p_x^{ij} \\ p_y^{ij} \\ m_x^{ij} \\ m_y^{ij} \end{pmatrix} \quad (23)$$

According to the Bloch theorem, the electric and magnetic dipole moments are connected with the ones for the nearest neighbors as

$$\begin{pmatrix} p_x^{i+1, j} \\ p_y^{i+1, j} \\ m_x^{i+1, j} \\ m_y^{i+1, j} \end{pmatrix} = e^{ik_x} \begin{pmatrix} p_x^{ij} \\ p_y^{ij} \\ m_x^{ij} \\ m_y^{ij} \end{pmatrix}, \quad \begin{pmatrix} p_x^{i-1, j} \\ p_y^{i-1, j} \\ m_x^{i-1, j} \\ m_y^{i-1, j} \end{pmatrix} = e^{-ik_x} \begin{pmatrix} p_x^{ij} \\ p_y^{ij} \\ m_x^{ij} \\ m_y^{ij} \end{pmatrix} \quad (24)$$

$$\begin{pmatrix} p_x^{i, j+1} \\ p_y^{i, j+1} \\ m_x^{i, j+1} \\ m_y^{i, j+1} \end{pmatrix} = e^{ik_y} \begin{pmatrix} p_x^{ij} \\ p_y^{ij} \\ m_x^{ij} \\ m_y^{ij} \end{pmatrix}, \quad \begin{pmatrix} p_x^{i, j-1} \\ p_y^{i, j-1} \\ m_x^{i, j-1} \\ m_y^{i, j-1} \end{pmatrix} = e^{-ik_y} \begin{pmatrix} p_x^{ij} \\ p_y^{ij} \\ m_x^{ij} \\ m_y^{ij} \end{pmatrix} \quad (25)$$

The right hand side of Eq. (23) can be rewritten in the form:

$$\begin{pmatrix} u & 0 & 0 & -iv \\ 0 & u & iv & 0 \\ 0 & -iv & u & 0 \\ iv & 0 & 0 & u \end{pmatrix} \begin{pmatrix} p_x^{nl} \\ p_y^{nl} \\ m_x^{nl} \\ m_y^{nl} \end{pmatrix} = u \begin{pmatrix} 1 & 0 & 0 & 0 \\ 0 & 1 & 0 & 0 \\ 0 & 0 & 1 & 0 \\ 0 & 0 & 0 & 1 \end{pmatrix} \begin{pmatrix} p_x^{nl} \\ p_y^{nl} \\ m_x^{nl} \\ m_y^{nl} \end{pmatrix} + iv \begin{pmatrix} 0 & 0 & 0 & -1 \\ 0 & 0 & 1 & 0 \\ 0 & -1 & 0 & 0 \\ 1 & 0 & 0 & 0 \end{pmatrix} \begin{pmatrix} p_x^{nl} \\ p_y^{nl} \\ m_x^{nl} \\ m_y^{nl} \end{pmatrix} \quad (26)$$

In the following, we rely on the approximations  $u = \frac{\omega - \omega_0}{\text{const}}$ , where  $\omega_0$  is the resonant frequency of a resonator, and  $v = \text{const}$  [1]. To convert the equation to dimensionless values, we set  $q = ak_0$ ,  $\mu = 2va^3$ , and  $E = 2a^3 \frac{\omega - \omega_0}{\text{const}}$ . Then,

$$u \widehat{I}_4 \begin{pmatrix} p_x^{ij} \\ p_y^{ij} \\ m_x^{ij} \\ m_y^{ij} \end{pmatrix} + iv \begin{pmatrix} 0 & 0 & 0 & -1 \\ 0 & 0 & 1 & 0 \\ 0 & -1 & 0 & 0 \\ 1 & 0 & 0 & 0 \end{pmatrix} \begin{pmatrix} p_x^{ij} \\ p_y^{ij} \\ m_x^{ij} \\ m_y^{ij} \end{pmatrix} \equiv \frac{E}{2a^3} \widehat{I}_4 \begin{pmatrix} p_x^{ij} \\ p_y^{ij} \\ m_x^{ij} \\ m_y^{ij} \end{pmatrix} + \frac{i\mu}{2a^3} \begin{pmatrix} 0 & 0 & 0 & -1 \\ 0 & 0 & 1 & 0 \\ 0 & -1 & 0 & 0 \\ 1 & 0 & 0 & 0 \end{pmatrix} \begin{pmatrix} p_x^{ij} \\ p_y^{ij} \\ m_x^{ij} \\ m_y^{ij} \end{pmatrix} \quad (27)$$

where  $\hat{I}_4$  is the  $[4 \times 4]$  unity matrix. Finally Eq. (23) can be presented as:

$$\left[ 2a^3(e^{ik_x} + e^{-ik_x}) \begin{pmatrix} A, 0, 0, 0 \\ 0, B, 0, 0 \\ 0, 0, A, 0 \\ 0, 0, 0, B \end{pmatrix} + 2a^3(e^{ik_y} + e^{-ik_y}) \begin{pmatrix} B, 0, 0, 0 \\ 0, A, 0, 0 \\ 0, 0, B, 0 \\ 0, 0, 0, A \end{pmatrix} - i\mu \begin{pmatrix} 0 & 0 & 0 & -1 \\ 0 & 0 & 1 & 0 \\ 0 & -1 & 0 & 0 \\ 1 & 0 & 0 & 0 \end{pmatrix} \right] \begin{pmatrix} p_x^{ij} \\ p_y^{ij} \\ m_x^{ij} \\ m_y^{ij} \end{pmatrix} = E\hat{I}_4 \begin{pmatrix} p_x^{ij} \\ p_y^{ij} \\ m_x^{ij} \\ m_y^{ij} \end{pmatrix}. \quad (28)$$

In the following, we consider near-field contribution in Green's function exclusively. Also, we assume that  $q \ll 1$ , because  $\lambda \gg a$ , where  $\lambda$  is wavelength corresponding to the frequencies around 2.5 GHz. Thus, the exponent approximately equals  $\exp^{iq} \approx 1$ . Finally,  $a^3A \approx 2$  and  $a^3B \approx -1$ ,  $e^{ik} + e^{-ik} = 2 \cos k$ , and the derived Bloch Hamiltonian takes the form

$$\hat{H}(k_x, k_y) = \begin{pmatrix} 8 \cos k_x - 4 \cos k_y & 0 & 0 & i\mu \\ 0 & 8 \cos k_y - 4 \cos k_x & -i\mu & 0 \\ 0 & i\mu & 8 \cos k_x - 4 \cos k_y & 0 \\ -i\mu & 0 & 0 & 8 \cos k_y - 4 \cos k_x \end{pmatrix}. \quad (29)$$

With the help of Pauli matrices  $\hat{\sigma}_x = (0, 1; 1, 0)$ ,  $\hat{\sigma}_y = (0, -i; i, 0)$ , and  $\hat{\sigma}_z = (1, 0; 0, -1)$ , and  $[2 \times 2]$  unity matrix  $\hat{I}$ , the Bloch Hamiltonian can be rewritten as:

$$\hat{H}(k_x, k_y) = 2(\cos k_x + \cos k_y) \begin{pmatrix} \hat{I}_2 & 0 \\ 0 & \hat{I}_2 \end{pmatrix} + 6(\cos k_x - \cos k_y) \begin{pmatrix} \hat{\sigma}_z & 0 \\ 0 & \hat{\sigma}_z \end{pmatrix} - \mu \begin{pmatrix} 0 & \hat{\sigma}_y \\ \hat{\sigma}_y & 0 \end{pmatrix}. \quad (30)$$

To rewrite the derived Hamiltonian in a block-diagonal form, the basis  $|\psi\rangle = (p_x, p_y, m_x, m_y)^T$  should be replaced by  $|\psi'\rangle = (p_x + im_y, p_x - im_y, p_y - im_x, p_y + im_x)^T$ . Thus, the unitary transform matrix  $\hat{U}$  is

$$\begin{pmatrix} 1 & 0 & 0 & i \\ 1 & 0 & 0 & -i \\ 0 & 1 & -i & 0 \\ 0 & 1 & i & 0 \end{pmatrix}, \quad (31)$$

and the Hamiltonian takes the following form:

$$\hat{H}(k_x, k_y) = 2(\cos k_x + \cos k_y)\hat{I} \otimes \hat{I} - 2\mu\hat{I} \otimes \hat{\sigma}_z + 6(\cos k_x - \cos k_y)\hat{\sigma}_z \otimes \hat{\sigma}_x = \begin{pmatrix} \hat{H}^{(+)} & 0 \\ 0 & \hat{H}^{(-)} \end{pmatrix}. \quad (32)$$

#### SUPPLEMENTARY NOTE 4. EXPERIMENTAL EVALUATION OF THE DISPERSION DIAGRAM

To characterize the dispersion of the topological states at the interface, we put the source antenna at the edge of the domain wall and measure the excited magnetic field along the interface. Then, we evaluate the dynamic structure factor (DSF)  $S(k, f)$  by applying Fourier transform to the extracted array of frequency-dependent  $S_{21}$ -parameters measured at different spatial points:

$$S(k, f) = \sum_{j=0}^{N-1} S_{21}(y_j, f)e^{-iky_j} = \sum_{j=0}^{N-1} S_{21}(j, f)e^{-ik\Delta j/a}, \quad (33)$$

where  $S_{21}(y_j, f) \equiv S_{21}(j, f)$  is the transmission coefficient at the frequency  $f$  for the loop probe located at the point  $y_j = j\Delta$  mm along the interface and the exciting dipole antenna located at the point  $y = 0$  mm,  $\Delta = 2.5$  mm is the scanning step,  $N = 185$  is the total number of scanning points,  $a = 37.1$  mm is the structure period, and  $k \in [0, \pi]$  is the dimensionless wavenumber.

---

[1] Alexey A Gorlach, Dmitry V Zhirihin, Alexey P Slobozhanyuk, Alexander B Khanikaev, and Maxim A Gorlach, "Photonic Jackiw-Rebbi states in all-dielectric structures controlled by bianisotropy," [Physical Review B \*\*99\*\*, 205122 \(2019\)](#).